

Smoothened and ARL13B are critical in mouse for superior cerebellar peduncle targeting

Sarah K. Suciu^{*,†,‡} Alyssa B. Long^{†,‡} and Tamara Caspary[†]

*Genetics and Molecular Biology Graduate Program, †Department of Human Genetics,
Emory University, Atlanta, GA 30322, ‡These authors contributed equally

ORCID ID:

Suciu: 0000-0002-2416-9519

Long: 0000-0002-4467-4213

Caspary: 0000-0002-6579-7589

Summary statement

Joubert syndrome is diagnosed by the hindbrain “molar tooth sign” malformation. Using mouse models, we show loss of the ciliary GTPase ARL13B, mutations in which lead to Joubert syndrome, result in two features of the molar tooth sign: hypoplasia of the cerebellar vermis and inappropriate targeting of the superior cerebellar peduncles. Furthermore, we demonstrate that loss of vertebrate Hedgehog signaling may be the underlying disrupted mechanism as we extend its role in axon guidance to the superior cerebellar peduncles.

Running title (~35 characters, including spaces):

SMO and ARL13B in SCP targeting

Key words/phrases (up to ten):

molar tooth sign, Joubert syndrome, Smo, ARL13B, SCP targeting, cerebellar vermis

Corresponding author:

Tamara Caspary

Department of Human Genetics

615 Michael Street, Suite 301

Atlanta, GA 30322

404-727-9862

tcaspar@emory.edu

1 **Abstract**

2 Patients with the ciliopathy Joubert syndrome present with physical anomalies,
3 intellectual disability, and are diagnosed by the hindbrain “molar tooth sign”
4 malformation. This radiological abnormality results from a combination of hypoplasia of
5 the cerebellar vermis and inappropriate targeting of the white matter tracts of the
6 superior cerebellar peduncles, which create a deepened interpeduncular fossa. *ARL13B*
7 is a cilia-enriched regulatory GTPase established to regulate cell fate, cell proliferation
8 and axon guidance through vertebrate Hedgehog signaling. In patients, point mutations
9 in *ARL13B* cause Joubert syndrome. In order to understand the etiology of the molar
10 tooth sign, we used mouse models to investigate the role of *ARL13B* during cerebellar
11 development. We found *ARL13B* regulates superior cerebellar peduncle targeting and
12 these fiber tracts require Hedgehog signaling for proper guidance. However, in mouse
13 the Joubert-causing R79Q mutation in *ARL13B* does not disrupt Hedgehog signaling
14 nor does it impact tract targeting. We found a small cerebellar vermis in mice lacking
15 *ARL13B* function but no cerebellar vermis hypoplasia in mice expressing the Joubert-
16 causing R79Q mutation. Additionally, mice expressing a cilia-excluded variant of
17 *ARL13B* that transduces Hedgehog normally, showed normal tract targeting and vermis
18 size. Taken together, our data indicate that *ARL13B* is critical for superior cerebellar
19 peduncle targeting, likely via Hedgehog signaling, as well as control of cerebellar vermis
20 size. Thus, our work highlights the complexity of *ARL13B* in molar tooth sign etiology.

21 INTRODUCTION

22 Joubert Syndrome and Related Disorders (JSRD) are autosomal recessive
23 congenital disorders with a variety of symptoms including developmental delay,
24 intellectual disability, abnormal respiratory rhythms, ataxia, oculomotor apraxia,
25 polydactyly, craniofacial defects, retinal dystrophy, nephronophthisis, and hepatic
26 fibrosis (Parisi *et al.* 2007). While the exact prevalence of JSRD is not known, published
27 statistics range from 1:80,000 to 1:100,000, but these may be underestimates (Brancati
28 *et al.* 2010). The characteristic neuroanatomical feature of JSRD is the molar tooth sign
29 (MTS), which is caused by hypoplasia of the cerebellar vermis and thickened, elongated
30 superior cerebellar peduncles (SCPs) that fail to decussate (Yachnis and Rorke 1999;
31 Poretti *et al.* 2007). However, little is known about the etiology of this hindbrain
32 malformation. This is especially significant in light of the fact that many severe
33 symptoms of JSRD arise from defects in the hindbrain: cerebellar dysfunction
34 commonly causes ataxia, while life-threatening breathing problems are linked to
35 hindbrain nuclei such as the parafacial respiratory group and pre-Bötzing complex
36 (Onimaru *et al.* 2006).

37 To date, mutations in any of 35 genes cause JSRD, and their associated proteins
38 almost always localize to the primary cilium or the centrosome (Parisi 2019). Thus,
39 JSRD is classified as a ciliopathy, a category of human disease stemming from ciliary
40 dysfunction. One of the genes implicated in JSRD is *ARL13B*, which encodes a
41 regulatory GTPase highly enriched in cilia (Cantagrel *et al.* 2008; Bachmann-Gagescu
42 *et al.* 2015; Thomas *et al.* 2015; Shaheen *et al.* 2016; Rafiullah *et al.* 2017). As a
43 GTPase, *ARL13B* is expected to have multiple effector proteins which interact with

44 specific ARL13B residues. ARL13B can function as guanine exchange factor (GEF) for
45 ARL3, mutations in which also lead to JSRD (Gotthardt *et al.* 2015; Ivanova *et al.* 2017).
46 JSRD-causing mutations in either ARL3 or ARL13B can disrupt their interaction or
47 ARL13B's GEF activity, consistent with the notion that specific ARL13B function is
48 affected by JS-causing point mutations (Gotthardt *et al.* 2015; Ivanova *et al.* 2017;
49 Alkanderi *et al.* 2018). Most JSRD-causing ARL13B mutations cluster within the
50 protein's GTPase domain, although two are located in the coiled coil domains in the C
51 terminal half of the protein (Cantagrel *et al.* 2008; Bachmann-Gagescu *et al.* 2015;
52 Thomas *et al.* 2015; Shaheen *et al.* 2016; Rafiullah *et al.* 2017). ARL13B complexes
53 with the inositol phosphatase INPP5E, which is also implicated in causing JSRD (Bielas
54 *et al.* 2009; Humbert *et al.* 2012). ARL13B is critical for targeting INPP5E to cilia and
55 JSRD-causing ARL13B mutations disrupt INPP5E ciliary targeting (Humbert *et al.*
56 2012). INPP5E controls ciliary lipid composition through its phosphatase activity and
57 most JSRD-causing mutations are within its phosphatase domain (Bielas *et al.* 2009;
58 Chavez *et al.* 2015; Garcia-Gonzalo *et al.* 2015). Other proteins implicated in JSRD also
59 affect ciliary targeting with many functioning at the transition zone, supporting the notion
60 that abnormal ciliary traffic leading to defective signaling underlies JSRD (Arts *et al.*
61 2007; Delous *et al.* 2007; Garcia-Gonzalo *et al.* 2011; Hopp *et al.* 2011; Srour *et al.*
62 2012; Roberson *et al.* 2015).

63 The mechanistic connection between the cilia-related proteins implicated in
64 JSRD and the MTS are elusive. The hypoplastic cerebellar vermis and the abnormal
65 SCP tracts disrupt the distinct biological processes of proliferation and axonal targeting.
66 One signaling pathway potentially linked to both processes is vertebrate Hedgehog (Hh)

67 which relies on cilia (Huangfu *et al.* 2003). Sonic hedgehog (Shh) is a mitogenic cue
68 that controls proliferation in the developing cerebellum so its misregulation could
69 underlie the cerebellar hypoplasia (Dahmane and Ruiz i Altaba 1999; Wechsler-Reya
70 and Scott 1999; Kenney and Rowitch 2000). While the SCP tracts that normally project
71 from the deep cerebellar nuclei to the contralateral thalamus are guided by unknown
72 signals, Shh is a known commissural axon guidance cue (Charron *et al.* 2003). JSRD
73 patients also display axon guidance defects in decussation of pyramidal tracts and in
74 crossing of the tracts in the optic chiasm, the latter of which is a Shh-dependent process
75 (Fabre *et al.* 2010; Sanchez-Arrones *et al.* 2013).

76 The JSRD-causing genes *ARL13B* and *INPP5E* are known to regulate vertebrate
77 Hh signaling. In mouse models, *ARL13B* loss disrupts cell fate specification in the
78 neural tube, proliferation of the cerebellar granule precursor cells in the cerebellum and
79 Shh-directed guidance of commissural axons in the spinal cord (Caspary *et al.* 2007;
80 Bay *et al.* 2018; Ferent *et al.* 2019). These data support a model whereby disruption of
81 Shh signaling by *ARL13B* mutation could provide a single mechanism underlying the
82 MTS. This model is bolstered by the fact that additional phenotypes exhibited by JSRD
83 patients, such as craniofacial defects or polydactyly, can arise from aberrant Hh
84 signaling (Valente *et al.* 2008; Lan and Jiang 2009; Lipinski *et al.* 2010).

85 As attractive as a Hh-based model for JSRD may be, not all the data support that
86 JSRD phenotypes result from misregulation of Hh signaling. Some features of JSRD,
87 such as the renal and liver anomalies, are not clearly due to misregulation of Hh
88 signaling (Doherty 2009; Breslow *et al.* 2018). Additionally, of the 35 genes implicated in
89 JSRD, 22 have some role in Hh pathway regulation, even if indirectly (Hata *et al.* 2000;

90 Davey *et al.* 2006; Reiter and Skarnes 2006; Caspary *et al.* 2007; Vierkotten *et al.* 2007;
91 Tran *et al.* 2008; Huang *et al.* 2009; Weatherbee *et al.* 2009; Bimonte *et al.* 2011;
92 Dowdle *et al.* 2011; Sang *et al.* 2011; Chih *et al.* 2011; Christopher *et al.* 2012; Thomas
93 *et al.* 2012; Abdelhamed *et al.* 2013; Hynes *et al.* 2014; Wu *et al.* 2014; Garcia-Gonzalo
94 *et al.* 2015; Asadollahi *et al.* 2018; Frikstad *et al.* 2019; Munoz-Estrada and Ferland
95 2019; Casoni *et al.* 2020). Others, like *ARL3*, lack such evidence (Alkanderi *et al.* 2018).
96 *Arl3* mouse mutants do not exhibit any of the phenotypes exhibited by mutants in the Hh
97 pathway, suggesting that it may regulate Hh-independent pathways (Schrick *et al.*
98 2006). Indeed, additional signaling pathways are linked to cilia including others known
99 to be important in cell proliferation and axon guidance. Loss of either of the JSRD-linked
100 genes *Ahi1* or *Cep290* in mouse leads to a small cerebellar vermis due to aberrant Wnt
101 signaling (Lancaster *et al.* 2011; Ramsbottom *et al.* 2020). JSRD-causing mutations in
102 *Znf423* are linked to defects in Wnt, BMP and retinoic acid signaling (Hata *et al.* 2000,
103 Huang *et al.* 2009, Casoni *et al.* 2020, Deshpande *et al.* 2020). Conditional *Arl13b* or
104 *Inpp5e* deletion in the SCPs results in their disorganization and thickening through
105 misregulation of ciliary PI3 kinase and AKT (Guo *et al.* 2019).

106 Ciliopathies are well established to be genetically complex. JSRD patients with
107 different *ARL13B* mutations can display distinct phenotypes, such as ataxia in an
108 individual expressing *ARL13B*^{Y86C} and occipital encephalocele in a patient expressing
109 *ARL13B*^{R79Q} (Cantagrel *et al.* 2008; Thomas *et al.* 2015). This is further exemplified in
110 cases of related individuals carrying the same mutation but exhibiting different
111 phenotypes and even diagnoses. For example, JSRD-causing mutations in *TMEM67*
112 (*R208X*) and *TMEM216* (*R73H*) can also cause the more severe disease Meckel-

113 Gruber syndrome (Consugar *et al.* 2007; Otto *et al.* 2009; Valente *et al.* 2010).
114 Understanding the genetic modifiers underlying the phenotypic variation will be key to
115 understanding disease etiology as will understanding when and how relevant pathways
116 interact. In mouse models of the JSRD- and Meckel-Gruber Syndrome-linked gene
117 *Tmem67*, two phenotypic categories emerged: one with cerebellar malformations
118 resembling JSRD and another with more severe CNS defects reminiscent of Meckel-
119 Gruber syndrome (Abdelhamed *et al.* 2013). The two categories correlated with whether
120 cilia were retained, with the severe Meckel-Gruber-like phenotype observed in animals
121 lacking cilia. Furthermore, the two phenotypic groups impacted Hh and Wnt signaling
122 differently, pointing to both pathways being critical (Abdelhamed *et al.* 2019).
123 Importantly, it is not simply whether cilia are present, as another JSRD mouse model,
124 *Talpid3*, lacks cilia yet displays a JSRD-like small cerebellar vermis (Bashford and
125 Subramanian 2019). Thus, mouse models are incredibly informative yet point to the
126 enormous complexity underlying the MTS.

127 Here we investigate the role of ARL13B in relation to Hh signaling in two major
128 features of the MTS: targeting of the SCPs to the thalamus and hypoplasia of the
129 cerebellar vermis. We explore these processes using a series of mouse alleles through
130 which we first define the roles of Hh signaling and ARL13B in SCP projections.
131 Subsequently, we untangle the role of ARL13B from within and outside of the cilium and
132 investigate a JS-causing patient allele. Taken together, our data illuminate the roles of
133 ARL13B in MTS etiology and the complexity in modeling aspects of the MTS in mouse.

134

135 **MATERIALS & METHODS**

136 *Mouse lines*

137 All mice were cared for in accordance with NIH guidelines and Emory
138 University's Institutional Animal Care and Use Committee (IACUC). Lines used were
139 *Nex-Cre* (*Neurod6^{tm1(cre)Kan}*)-C3H/HeJ [MGI:2668659], *Brn4-Cre* (*Tg(Pou3f4-*
140 *cre)32Cren*)-C3H/HeJ [MGI:2158470], *Smo^{flox}* (*Smo^{tm2AMC}*)-C3H/HeJ [MGI:2176256],
141 *Arl13b^{flox}* (*Arl13b^{tm1Tc}*)-C3H/HeJ [MGI:4948239], *Arl13b^{V358A}*-C57Bl/6J (*Arl13b^{em1Tc}*)
142 [MGI:6256969], and *Arl13b^{R79Q}*-C57Bl/6J (*Arl13b^{em2Tc}*) [MGI:6279301]. Note that
143 *Arl13b^Δ* is the deletion allele resulting from germline deletion of the conditional *Arl13b^{flox}*
144 allele. Genotyping was as previously described (Heydemann *et al.* 2001; Goebbels *et*
145 *al.* 2006; Nolan-Stevaux *et al.* 2009; Su *et al.* 2012; Gigante *et al.* 2020).

146 To generate the R79Q mutation in *Arl13b*, a CRISPR gRNA
147 (ATTATTATGCTGAATCCTATGG) targeting exon 3 of the *Arl13b* locus along with a
148 donor oligo (5'-
149 GTTCCAAGTTACCATCTTTGACTTAGGAGGTGGAAAAGAATTCAGGGGCATATTGGA
150 AGAATTATTATGCTGAATCCTATGGGGTAATATTTGTTGTGGATTCCAGTGATGAGG
151 AGAGAAT-3'; underlined bases are engineered) were designed to generate a G-to-A
152 change creating the R79Q point mutation as well as A-to-C and T-to-A silent changes to
153 create a NdeI restriction site that could be used for genotyping (Millipore Sigma). The
154 gRNA (50 ng/ul), oligo donor (50 ng/ul) and CRISPR protein (100 ng/ul) were injected
155 into 1-cell C57Bl/6J zygotes and subsequently transplanted at the 2-cell stage into
156 C57Bl/6J pseudopregnant females by the Emory Transgenic and Gene Targeting Core.
157 Genomic DNA from toes was amplified via PCR using primers (5'-
158 TCACTTGCAACAGAGCATCC-3') and (5'-ACAGCTCTGCCCGTGTTTAC-3') located

159 upstream and downstream of the donor oligo breakpoints; products were sequenced
160 with the forward (first) primer. A single founder animal heterozygous for both the R79Q
161 mutation and NdeI restriction site was identified with no additional editing. Subsequent
162 allele-specific genotyping of progeny was performed on ear punch or yolk sac using the
163 following primers: Fwd-wt primer: 5'- GGAGGTGGAAAAGAATaCg-3'; Fwd-mut
164 primer: 5'-gctctatggctgGGAGGTGGAAAAGAATTga-3'; Rev primer: 5'-
165 AGTGCTAAGACACCCGAGGA-3'. PCR bands at 142bp (wild type) and/or 154bp
166 (mutant) were produced, due to the addition of 12 non-templated bases to the 5' end of
167 the Fwd-mut primer (lowercase). Note the 3' ends of the two forward primers differed in
168 the base that codes for the R to Q change (final nucleotide of the primer) and includes a
169 "wobble" base (lowercase) to provide allele-specific amplification after the first round of
170 PCR (Gaudet *et al.* 2009).

171

172 *Tract tracing injections and analysis*

173 Tract tracing experiments were performed according to a protocol approved by
174 Emory University's Institutional Animal Care and Use Committee (IACUC). Male and
175 female mice at postnatal day 90 or older were used for tract tracing experiments. At
176 least 3 mice of each genotypic group were analyzed in experiments (exact N included in
177 Figures 1-3). Mice were anesthetized with inhaled isoflurane and maintained under
178 anesthesia throughout the procedure. Animals were secured in the stereotax, and the
179 scalp was opened with bregma and lambda aligned to flatskull position. Dorsal thalamus
180 injections were targeted to the bregma (AP:-0.70, ML:+1.13, DV:-3.28, Angle:0°) and
181 ventral thalamus injections were targeted using coordinates to the bregma (AP:-0.70,

182 ML:-3.11, DV:-4.69, Angle:25°). Ventral injection targeting includes a 25° angle to avoid
183 pulling dye through the dorsal thalamus upon needle removal. Then, a 5 ul Hamilton
184 microsyringe was lowered to target and target was injected with lysine fixable dextran
185 tetramethylrhodamine neuroanatomical tracer (fluoro-Ruby, 10,000 MW, ThermoFisher
186 Scientific D1817). Animals received 0.05 - 0.5 ul injections of 10% dextran
187 tetramethylrhodamine in sterile phosphate buffered saline (PBS, pH = 7.25) unilaterally
188 at a rate of 0.1 ul/minute.

189 Seven days post-procedure, mice were perfused with 50mls of PBS followed by
190 30mls of 4% paraformaldehyde (PFA). Brains were kept in PFA overnight and
191 subsequently placed in 30% sucrose in 0.1M phosphate buffer (pH 7.3) for
192 cryoprotection for at least 48 hours. Brains were embedded in Tissue-Tek OCT
193 compound (Sakura) for coronal cryostat sectioning. Sections were 60 microns thick and
194 processed through 70% ethanol dehydration and 0.1% sudan black autofluorescence
195 quencher, rehydrated in PBS and treated with DAPI to stain nuclei prior to fluorescence
196 imaging. Images were taken on a Lionheart FX automated microscope (Biotek) or at 5x
197 magnification on a Leica DM6000B microscope (Leica) using SimplePCI imaging
198 software (Hamamatsu). The Leica images were subsequently stitched together to reveal
199 the entirety of the brain section in Fiji (Schindelin *et al.* 2012) or Photoshop (Adobe).
200 Surgical injection sites were assessed to ensure dye was present at the desired
201 injection site. If the injection was off-target or dye at the injection site was not seen,
202 samples were removed from analysis. Cerebellar images from injections were evaluated
203 for DCN staining with assessor blinded to genotype. The number of injections that
204 resulted in fluorescent DCN for each injection site (dorsal and ventral thalamus) were

205 compared between mutant and control genotypes using a two-sided Fisher's exact test
206 (PRISM 8.2.0).

207

208 *Phenotypic analysis of embryos*

209 Timed matings of mice were performed to generate somite-matched embryos at
210 embryonic day 10.5 (E10.5). Embryos were dissected in cold PBS and processed for
211 immunofluorescence staining as previously described (Constable *et al.* 2020). Primary
212 antibodies used were: mouse anti-Shh (5E1, 1:10), mouse anti-Pax6 (PAX6, 1:100)
213 (Developmental Studies Hybridoma Bank), and rabbit anti-Olig2 (AB9610, 1:500,
214 Millipore Sigma). Multiple sections from three embryos of each genotype were
215 examined.

216

217 *Analysis of cerebellar vermis width*

218 Weanling age (P20-P24) male and female mice were sacrificed and brains were
219 harvested and fixed in 4% PFA overnight at 4°. Ten sex-matched pairs of mouse brains
220 were collected for each genotype, which is sufficiently powered to detect differences as
221 small as 3% (Deshpande *et al.* 2020). Brains were imaged on a tilted stage to present a
222 surface view of the cerebellum, with a standard ruler in frame to confirm scale, using a
223 dissecting microscope (Leica MZFLIII). Measurements were made in FIJI (Schindelin *et*
224 *al.* 2012) with the investigator blind to genotype. Whole cerebellar width was measured
225 at the widest part of the cerebellum, coinciding with lobule CI or CII. Vermis width was
226 calculated by measuring the widest part of lobule VII (Deshpande *et al.* 2020). For each
227 sex- and age-matched pair, the ratio of mutant to control width was calculated and a

228 one-sample t-test was performed and compared to a hypothetical value of 1 (PRISM
229 8.2.0). All of our sample groups passed the Shapiro-Wilk test for normality.

230

231 **Data availability**

232 Mouse lines are available upon request. The authors affirm that all data
233 necessary for confirming the conclusions of the article are present within the article and
234 figures.

235

236 **RESULTS**

237 *SMO is required for normal SCP projection to the dorsal thalamus*

238 In order to test whether proper projection of SCPs requires Hh signaling, we
239 compared the SCP tracts in mice in which we deleted the gene encoding the obligate
240 Hh transducer, *Smoothened* (*Smo*), to control animals. As *Smo* null embryos die during
241 embryogenesis, we deleted *Smo* specifically in the projection neurons by generating
242 *Nex-Cre;Smo^{fl/fl}* mice, which we refer to as *Smo^{Nex-Cre}* (Zhang *et al.* 2001; Caspary *et al.*
243 2002). *Nex-Cre* initiates CRE recombinase expression at E11.5, as the precursor cells
244 of the deep cerebellar nuclei (DCN) begin to migrate and become specified (Fink *et al.*
245 2006; Goebbels *et al.* 2006). In the mature cerebellum, the SCPs project rostrally from
246 the DCN (illustrated in Figure 1A). After entering the midbrain, the SCPs cross the
247 midline and again turn rostrally to project to two positions in the rostral thalamus: one
248 tract takes a slight dorsal path and the other tract remains in the same plane; for
249 simplicity here, we term these projection sites the dorsal and ventral thalamus,
250 respectively (Bohne *et al.* 2019). To examine the SCP tracts, we used retrograde tract

251 tracing in which we performed stereotaxic injections of a lipophilic dextran dye into
252 either the dorsal or ventral thalamus and allowed the dye to diffuse through the axons to
253 the associated neuron's cell body (~7 days); we then sacrificed the animal and
254 examined the cerebellum for evidence of the lipophilic dye indicating tracing.

255 We found that both dorsal and ventral thalamus injections resulted in visible
256 clusters of dye-stained cells in the contralateral DCN, and not the ipsilateral DCN, in
257 control animals indicating the retrograde tract tracing reliably labelled the SCPs in our
258 hands (Figure 1D-E, dorsal: 6/8; ventral: 8/11). In the *Smo^{Nex-Cre}* mice, the results
259 differed depending on whether we injected in the dorsal or ventral thalamus (Figure 1F-
260 G). In the ventral thalamus injections, we detected dye-stained clusters of cells in the
261 contralateral DCN but not the ipsilateral DCN, indicating normal SCP projection to the
262 ventral thalamus (Figure 1G, 4/4 injections). This indicates that at least some SCPs
263 cross the midline. In the dorsal thalamus injections, we could not detect dye-stained
264 clusters of cells in either the contralateral or ipsilateral DCN (Figure 1F, 0/6 injections)
265 suggesting that SCPs lacking SMO do not project to the dorsal thalamus. These data
266 implicate SMO as critical for proper projection of the SCPs to the dorsal thalamus.

267

268 *ARL13B is required for normal SCP projection to the dorsal thalamus*

269 Given that ARL13B regulates vertebrate Hh signaling in a variety of contexts, we
270 next assessed ARL13B's role in proper SCP projection. In order to delete *ARL13B*
271 specifically in projection neurons, we generated *Nex-Cre;Arl13b^{fl/fl}* mice, which we refer
272 to as *Arl13b^{Nex-Cre}*. We performed dorsal and ventral thalamus injections for retrograde
273 tract tracing to examine the SCPs (Figure 1H-I). In the ventral thalamus injections of

274 *Arl13b^{Nex-Cre}* mice, we found dye-stained clusters of cells in the contralateral DCN
275 consistent with normal SCP projections crossing the midline and projecting to the
276 ventral thalamus (Figure 1I, 4/4 injections). In contrast, in the dorsal thalamus injections
277 of *Arl13b^{Nex-Cre}* mice, we generally did not detect dye-stained clusters of cells in either
278 the contralateral or ipsilateral DCN, suggesting that the SCPs lacking ARL13B do not
279 project to the dorsal thalamus (Figure 1H, 1/7 injections). These data link ARL13B
280 function to normal SCP projection. Furthermore, they reveal the same phenotype in
281 *Smo^{Nex-Cre}* and *Arl13b^{Nex-Cre}* mice.

282

283 *ARL13B does not function from within cilia to mediate SCP guidance*

284 *ARL13B* and the other 35 genes implicated in Joubert syndrome associate with
285 the cilium or centrosome leading to the assumption that protein dysfunction from these
286 locales underlies JSRD phenotypes (Parisi 2019). To directly ask whether ARL13B
287 mediates SCP guidance to the dorsal thalamus from within cilia, we examined a mouse
288 expressing a cilia-excluded variant of ARL13B, ARL13B^{V358A} (Figure 2) (Gigante *et al.*
289 2020). We previously demonstrated that ARL13B^{V358A} retains all known ARL13B
290 biochemical activity, is undetectable in cilia yet transduces vertebrate Hh signaling
291 normally (Mariani *et al.* 2016; Gigante *et al.* 2020). We found that either dorsal or ventral
292 thalamus injections resulted in visible clusters of dye-stained cells in the contralateral
293 DCN in control (Figure 2A-B, dorsal: 3/3; ventral: 5/5) and *Arl13b^{V358A/V358A}* (Figure 2C-
294 D, dorsal: 3/3; ventral: 3/3) animals. In the context of the previous result showing that
295 *Arl13b^{Nex-Cre}* mice display abnormal SCP projections to the dorsal thalamus, these data

296 demonstrate that ARL13B does not function from within cilia to regulate SCP
297 projections.

298

299 *SCP projection in mice expressing a Joubert-causing allele, Arl13b^{R79Q}*

300 In order to understand the relationship between ARL13B and MTS formation in
301 Joubert syndrome, we generated a mouse expressing the JSRD-causing R79Q
302 mutation. We used CRISPR/Cas9 editing to change the conserved residue in the
303 mouse genome. This amino acid change disrupts ARL13B's GEF activity for ARL3
304 (Gotthardt *et al.* 2015; Ivanova *et al.* 2017). We found *Arl13b^{R79Q/R79Q}* mice were viable
305 and fertile. We bred the *Arl13b^{R79Q}* allele to the null *Arl13b^Δ* allele to make *Arl13b^{R79Q/Δ}*
306 animals, which we found survived to adulthood. As *Arl13b^{Δ/Δ}* are embryonic lethal, this
307 genetically demonstrates that *Arl13b^{R79Q}* is a hypomorphic allele of *ARL13B* (Su *et al.*
308 2012).

309 To assess the role of ARL13B^{R79Q} in SCP guidance, we performed dorsal and
310 ventral thalamus dye injections in control and *Arl13b^{R79Q/R79Q}* mice (Figure 3). We
311 identified visible clusters of dye-stained cells in the contralateral DCN in control (Figure
312 3A-B, dorsal: 4/4; ventral: 3/3) and *Arl13b^{R79Q/R79Q}* (Figure 3C-D, dorsal: 3/3; ventral:
313 3/4) animals. Thus, despite the constitutive expression of the JSRD-causing allele
314 throughout development, we did not detect a SCP projection defect in the
315 *Arl13b^{R79Q/R79Q}* mouse model. In the context of the abnormal SCP projections to the
316 dorsal thalamus that we identified in the *Smo^{Nex-Cre}* and *Arl13b^{Nex-Cre}* mice, this result
317 indicates that the *Arl13b^{R79Q}* allele does not disrupt SMO function or any ARL13B
318 function that regulates SMO.

319

320 *Arl13b^{R79Q/R79Q} mice display normal Shh signal transduction in neural tube patterning*

321 To further investigate the role of the *Arl13b^{R79Q}* allele in Hh signaling, we
322 examined embryonic neural patterning as it is exquisitely sensitive to alterations in Shh
323 activity (Chiang *et al.* 1996; Briscoe and Ericson 1999). We generated E10.5 embryos
324 and stained neural tube sections with antibodies against Shh, Olig2 and Pax6 (Figure
325 4). As expected in wild type embryos, we observed Shh expression in the ventral-most
326 cells (the floorplate), Olig2 expression in lateral cells and Pax6 expression more
327 dorsally. We also saw the established abnormal cell fates in null *Arl13b^{Δ/Δ}* embryos: loss
328 of Shh staining in the floorplate (Figure 4D), dorsal and ventral expansion of Olig2
329 expression (Figure 4H), and a dorsal shift in Pax6 expression (Figure 4L). We found
330 both *Arl13b^{R79Q/R79Q}* (Figure 4B, F, J) and *Arl13b^{R79Q/Δ}* (Figure 4C, G, K) embryos
331 displayed neural patterning indistinguishable from wild type embryos, indicating the
332 *Arl13b^{R79Q}* allele is not dosage-sensitive and does not disrupt Shh signaling in
333 determining neural cell fate.

334

335 *Arl13b^{R79Q/R79Q} mice display normal cerebellar size*

336 The lack of a SCP projection phenotype in the *Arl13b^{R79Q/R79Q}* mice surprised us
337 since JS patients display the MTS. In addition to defects in the SCPs, the MTS is due to
338 an underdeveloped cerebellar vermis, so we examined the size of the cerebellum and
339 the cerebellar vermis (Figure 5) (Aguilar *et al.* 2012). To quantify cerebellar size, we
340 performed analysis of surface-facing anatomical measurements validated to be
341 sufficiently sensitive to detect small differences in cerebellar vermis size (Deshpande *et*

342 *al.* 2020). Briefly, we measured cerebellar width as well as cerebellar vermis width
343 (widest part of lobule VII) of fixed whole mount dissected brains. For each sex- and age-
344 matched pair, we calculated the ratio of the width measurements from mutant to control,
345 which we compared to a hypothetical value of 1 (indicating no difference between
346 groups). We detected no differences in the overall cerebellar width or the cerebellar
347 vermis width between control and *Arl13b*^{R79Q/R79Q} mice of either sex (Figure 5B, C).
348 Thus, unlike patients carrying *ARL13B*^{R79Q/R79Q}, *Arl13b*^{R79Q/R79Q} mice do not display a
349 detectable growth deficit in the cerebellar vermis.

350

351 *Global cerebellar hypoplasia is observed in mice lacking Ar13b in all neurons*

352 Cerebellar size is well established to be regulated, in part, via Shh signaling
353 which controls proliferation of the cerebellar granule precursor cells (Kenney and
354 Rowitch 2000; Chizhikov *et al.* 2007). In order to better understand the cerebellar size
355 phenotype seen in JBTS patients in relation to ARL13B, we wanted to investigate how
356 ARL13B regulates cerebellar size. To do so, we crossed the *Brn4-Cre* allele into the
357 conditional null *Arl13b*^{fl/fl} background, called *Arl13b*^{Brn4-Cre} (Figure 6). *Brn4-Cre* initiates
358 expression at E8.5 throughout the neuroectoderm so the cerebellum develops in the
359 absence of ARL13B (Heydemann *et al.* 2001; Hazen *et al.* 2012). *Arl13b*^{Brn4-Cre} mice
360 develop hydrocephaly just after weaning which often leads to death. We again
361 calculated width ratios using surface-facing anatomical measurements and found the
362 overall width of the cerebellum was 6% reduced in both females and males lacking
363 ARL13B compared to control littermates at weaning (Figure 6B, p<0.05). More striking,
364 in the cerebellar vermis we detected a 27% reduction in width in female and a 33%

365 reduction in male mutants compared to controls (Figure 6C, $p < 0.0001$). From these
366 data, we conclude that loss of *ARL13B* leads to a modest global cerebellar size deficit
367 and a more pronounced cerebellar vermis size reduction.

368

369 *Arl13b*^{V358A/V358A} mice display normal cerebellar size

370 JS is classified as a ciliopathy due to the majority of causative genes encoding
371 proteins that, like *ARL13B*, are associated with cilia. In order to better understand the
372 role of ciliary *ARL13B* in cerebellar size, we examined cerebellar width in the mice
373 expressing the cilia-excluded variant *ARL13B*^{V358A} (Figure 7) (Gigante *et al.* 2020). We
374 detected no difference in the overall cerebellar width or that of the cerebellar vermis
375 between control and *Arl13b*^{V358A/V358A} mice (Figure 7B, C). Thus, *ARL13B* does not
376 control cerebellar size from within cilia.

377

378 **DISCUSSION**

379 Here we demonstrate that complete loss of *Arl13b* function in mouse can account
380 for two aspects of the MTS: aberrant SCP thalamic targeting and cerebellar vermis
381 hypoplasia. We expand the role of Hh signaling as a critical guidance cue by showing it
382 is required for proper SCP projection to the dorsal thalamus. Our finding that the SCP
383 phenotype is identical in *Smo*^{Nex-Cre} and *Arl13b*^{Nex-Cre} mice is consistent with a model
384 whereby *ARL13B* regulates SCP projections to the dorsal thalamus via a SMO-
385 dependent mechanism. In line with previous work showing that *ARL13B* does not
386 function from within cilia to regulate Shh-guided axon guidance, we found normal SCP
387 thalamic targeting in mice expressing only a cilia-excluded *ARL13B* variant (Feret *et al.*

388 2019). By mutating a conserved arginine to glutamine, we generated a mouse
389 expressing a mutation linked to JSRD in humans and observed no change in vertebrate
390 Hh signaling (Cantagrel *et al.* 2008). Additionally, we identified no defects in
391 *Arl13b*^{R79Q/R79Q} SCP projections. Whereas complete ARL13B deletion (*Arl13b*^{Bm4-Cre}) in
392 the cerebellum led to global hypoplasia, we show the cerebellum of *Arl13b*^{R79Q/R79Q} mice
393 is not significantly different in size compared to controls.

394 Overall, our data indicate ARL13B function is critical for both SCP targeting and
395 controlling cerebellar vermis size. At one level, our data implicate Hh signaling in the
396 etiology of the MTS since we show that SCP targeting requires SMO. However, at
397 another level, our data indicate that Hh-independent pathways are at play as we don't
398 observe Hh-dependent neural tube patterning defects in the presence of the JSRD-
399 causing *Arl13b*^{R79Q} allele. In other mouse models of JSRD where the hypoplasia is
400 specific to the cerebellar vermis, Wnt signaling is affected (Lancaster *et al.* 2011). Thus,
401 the MTS could be due to disruption of different pathways in the SCPs and the vermis.
402 This would imply that the 35 JSRD implicated genes all affect the distinct pathways in a
403 similar manner (Parisi 2019). Alternatively, the MTS may form due to alterations in any
404 of a few pathways - and it is even possible that alterations in one pathway could impact
405 other pathways - or the ability of cells to respond to those other pathways. Such a
406 model is hinted at by previous work showing interplay between the Hh and Wnt
407 pathways underlying the severity of hindbrain phenotypes (Hagemann and Scholpp
408 2012; Bashford and Subramanian 2019). While we haven't detected any changes in
409 Wnt response in the absence of ARL13B function, we may have not examined the
410 relevant biological process or used a sensitive enough readout (Horner and Casparly

411 2011). Parallel reasoning would thus suggest that while *Arl13b*^{R79Q/R79Q} mice clearly
412 transduce Hh reasonably well, there may be subtle changes in Shh signaling or
413 changes that influence Wnt signaling. Our data are consistent with the complexity
414 exhibited by other JSRD mouse models examined to date (Delous *et al.* 2007; Garcia-
415 Gonzalo *et al.* 2011; Roberson *et al.* 2015; Bashford and Subramanian 2019).

416 In patients, the SCP targeting deficit is more severe than what we observed in
417 the mice. The SCPs in patients do not cross the midline, appearing thickened on the
418 ipsilateral side relative to their DCN (Yachnis and Rorke 1999; Poretti *et al.* 2007).
419 However, in the mouse we infer midline crossing of the SCPs. In the case of the
420 *Smo*^{Nex-Cre} conditional mice, it is formally possible that the SCPs do not rely on SMO for
421 midline crossing but only for subsequent targeting to the dorsal thalamus. The fact that
422 the *Arl13b*^{Nex-Cre} conditional mice phenocopied the *Smo*^{Nex-Cre} phenotype makes this
423 less likely, since ARL13B is directly implicated in JSRD and regulates SMO-dependent
424 axon guidance in other contexts (Cantagrel *et al.* 2008; Ferent *et al.* 2019). It is also
425 plausible that the protein turnover driven by *Nex-Cre* completed after midline crossing
426 occurred. *Nex-Cre* expression initiates at E11.5 in the cells on the rhombic lip of the
427 cerebellar anlage as they start to migrate and be specified before occupying the deep
428 cerebellar nuclei (Fink *et al.* 2006; Goebbels *et al.* 2006). We expect deletion would
429 occur in the precursors and therefore the neurons of the DCN would not express
430 protein. Finally, it is possible that the mouse is not a valid system in which to model the
431 SCP midline crossing defect. This might explain why we saw no defects in the SCP
432 targeting of the *Arl13b*^{R79Q/R79Q} mice, as this is a constitutive mutation that requires no
433 protein turnover, yet homozygous expression of ARL13B^{R79Q} in patients results in the

434 molar tooth sign, which has been associated with failed decussation of white matter
435 tracts (Quisling *et al.* 1999). Indeed, other mouse mutants such as *Cep290* and *Ahi1*
436 which recapitulate the cerebellar vermis hypoplasia, also do not display midline crossing
437 defects in the SCPs (Lancaster *et al.* 2011). Whether this is due to anatomical
438 distinctions between the cerebellum in mouse and human or the genetic background on
439 which these models were examined are open questions. Recent work highlights clear
440 molecular and temporal differences between mouse and human cerebellar development
441 (Haldipur *et al.* 2019; Behesti *et al.* 2021).

442 Examining SCP projections is labor intensive and it has not been done
443 systematically among the JSRD mouse models (Bashford and Subramanian 2019; Guo
444 *et al.* 2019). While previous work showed that *Arl13b^{Nex-Cre}* and *Inpp5e^{Nex-Cre}* mice
445 exhibit SCP targeting deficits, here we pinpoint the *Arl13b^{Nex-Cre}* defect as specific to the
446 projection to the dorsal thalamus (Guo *et al.* 2019). The projection to the ventral
447 thalamus remains intact, suggesting there is not a generalized deficit in axon outgrowth
448 within the tract. The work on the *Arl13b^{Nex-Cre}* and *Inpp5e^{Nex-Cre}* SCP targeting deficits
449 argue that PI3K/Akt signaling from within cilia led to the tract defects (Guo *et al.* 2019).
450 However, we found that cilia-excluded ARL13B mediated SCP targeting normally.
451 These conflicting results could be explained by differences in the experimental details
452 as the data supporting ciliary ARL13B function used viral rescue whereas we used
453 genetic mutations engineered at the endogenous locus in this study. Alternatively, these
454 data could indicate that ARL13B plays an important cellular role in the ciliary trafficking
455 of key components needed for the PI3K/Akt pathways.

456 JSRD-causing mutations in ARL13B are generally restricted to the GTPase
457 domain of the protein, although two residues outside that domain are implicated in
458 disease (Cantagrel *et al.* 2008; Bachmann-Gagescu *et al.* 2015; Thomas *et al.* 2015;
459 Shaheen *et al.* 2016; Rafiullah *et al.* 2017). Based on other ARL proteins, ARL13B likely
460 assumes distinct conformations upon the binding either GDP or GTP, permitting
461 different binding partners or altering affinities for binding partners (Pasqualato *et al.*
462 2002; Miertzschke *et al.* 2014). None of the tested JSRD-causing mutations (R79Q,
463 Y86C or R200C) disrupt GTP binding or hydrolysis, however, all three mutations disrupt
464 ARL13B function as an ARL3 GEF (Ivanova *et al.* 2017). Given that complete deletion
465 of ARL13B impacts broader biological processes in the cerebellum than the R79Q
466 mutation and that the null mutant misregulates Hh signaling whereas R79Q does not,
467 we conclude that a subset of ARL13B function is disrupted in JSRD.

468

469 **Acknowledgements**

470 We are grateful to L. Mariani for her initial work on this project as well as R.E. Van
471 Sciver and E. Gigante for critical comments on the manuscript.

472

473 **Funding**

474 This work was supported by funding from National Institutes of Health grants
475 R01NS090029, R01GM110663 and R35GM122549 to T.C. and T32GM008490 and
476 F31NS101806 to S.K.S. with additional support from the Emory University Integrated
477 Cellular Imaging Microscopy Core of the Emory Neuroscience NINDS Core Facilities
478 grant, P30NS055077. This study was supported in part by the Mouse Transgenic and

479 Gene Targeting Core (TMF), which is subsidized by the Emory University School of
480 Medicine and is one of the Emory Integrated Core Facilities. Additional support was
481 provided by the National Center for Advancing Translational Sciences of the National
482 Institutes of Health under Award Number UL1TR000454. The content is solely the
483 responsibility of the authors and does not necessarily reflect the official views of the
484 National Institutes of Health.

485

486 ***Conflicts of Interest***

487 The authors have no competing interests to declare.

488

489 ***Author contributions statement***

490 Author Contributions: Conceptualization T.C.; Methodology S.K.S. and A.B.L.;
491 Validation S.K.S. and A.B.L.; Formal Analysis S.K.S. and A.B.L.; Investigation S.K.S.
492 and A.B.L.; Writing – Original Draft S.K.S. and T.C.; Writing – Review & Editing S.K.S.,
493 A.B.L. and T.C.; Visualization S.K.S. and A.B.L.; Supervision T.C.; Project
494 Administration T.C.; Funding Acquisition T.C.

495

496 ***References***

497 Abdelhamed, Z. A., D. I. Abdelmottaleb, M. E. El-Asrag, S. Natarajan, G. Wheway et al.,
498 2019 The ciliary Frizzled-like receptor Tmem67 regulates canonical Wwnt/beta-
499 catenin signalling in the developing cerebellum via Hoxb5. *Sci Rep.* **9**: 5446.
500 doi:10.1038/s41598-019-41940-5

- 501 Abdelhamed, Z. A., G. Wheway, K. Szymanska, S. Natarajan, C. Toomes et al., 2013
502 Variable expressivity of ciliopathy neurological phenotypes that encompass
503 Meckel-Gruber syndrome and Joubert syndrome is caused by complex de-
504 regulated ciliogenesis, Shh and Wnt signalling defects. *Hum Mol Genet.* **22**:
505 1358-1372. doi:10.1093/hmg/dds546
- 506 Aguilar, A., A. Meunier, L. Strehl, J. Martinovic, M. Bonniere et al., 2012 Analysis of
507 human samples reveals impaired SHH-dependent cerebellar development in
508 Joubert syndrome/Meckel syndrome. *Proc Natl Acad Sci U S A.* **109**: 16951-
509 16956. doi:10.1073/pnas.1201408109
- 510 Alkanderi, S., E. Molinari, R. Shaheen, Y. Elmaghloob, L. A. Stephen et al., 2018 ARL3
511 mutations cause Joubert syndrome by disrupting ciliary protein composition. *Am*
512 *J Hum Genet.* **103**: 612-620. doi:10.1016/j.ajhg.2018.08.015
- 513 Arts, H. H., D. Doherty, S. E. C van Beersum, M. A. Parisi, S. J. F. Letteboer et al., 2007
514 Mutations in the gene encoding the basal body protein RPGRIP1L, a
515 nephrocystin-4 interactor, cause Joubert syndrome. *Nat Genet.* **39**: 882-888.
516 doi:10.1038/ng2069
- 517 Asadollahi, R., J. E. Strauss, M. Zenker, O. Beuing, S. Edvardson et al., 2018 Clinical
518 and experimental evidence suggest a link between KIF7 and C5orf42-related
519 ciliopathies through Sonic Hedgehog signaling. *Eur J Hum Genet.* **26**: 197-209.
520 doi:10.1038/s41431-017-0019-9
- 521 Bachmann-Gagescu, R., J. C. Dempsey, I. G. Phelps, B. J. O'Roak, D. M. Knutzen et
522 al., 2015 Joubert syndrome: A model for untangling recessive disorders with

- 523 extreme genetic heterogeneity. *J Med Genet.* **52**: 514-522.
- 524 doi:10.1136/jmedgenet-2015-103087
- 525 Bashford, A. L., and V. Subramanian, 2019 Mice with a conditional deletion of Talpid3
526 (KIAA0586) - a model for Joubert syndrome. *J Pathol.* **248**: 396-408.
- 527 doi:10.1002/path.5271
- 528 Bay, S.N., A. B. Long, and T. Caspary, 2018 Disruption of the ciliary GTPpase Arl13b
529 suppresses Sonic hedgehog overactivation and inhibits medulloblastoma
530 formation. *Proc Natl Acad Sci U S A.* **115**: 1570-1575.
- 531 doi:10.1073/pnas.1706977115
- 532 Behesti, H. A. Kocabas, D. E. Buchholz, T. S. Carroll, and M. E. Hatten, 2021 Altered
533 temporal sequence of transcriptional regulators in the generation of human
534 cerebellar granule cells. bioRxiv. doi:10.1101/2021.01.17.427030 (Preprint
535 posted January 17, 2021).
- 536 Bielas, S. L., J. L. Silhavy, F. Brancati, M. V. Kisseleva, L. Al-Gazali et al., 2009
537 Mutations in INPP5E, encoding inositol polyphosphate-5-phosphatase E, link
538 phosphatidyl inositol signaling to the ciliopathies. *Nat Genet.* **41**: 1032-1036.
- 539 doi:10.1038/ng.423
- 540 Bimonte, S., A. De Angelis, L. Quagliata, F. Giusti, R. Tammaro et al., 2011 Ofd1 is
541 required in limb bud patterning and endochondral bone development. *Dev Biol.*
542 **349**: 179-191. doi:10.1016/j.ydbio.2010.09.020
- 543 Bohne, P., M. K. Schwarz, S. Herlitze, and M. D. Mark, 2019 A new projection from the
544 deep cerebellar nuclei to the hippocampus via the ventrolateral and laterodorsal
545 thalamus in mice. *Front Neural Circuits.* **13**: 51. doi:10.3389/fncir.2019.00051

- 546 Brancati, F., B. Dallapiccola, and E. M. Valente, 2010 Joubert syndrome and related
547 disorders. *Orphanet J Rare Dis.* **5**: 20. doi:10.1186/1750-1172-5-20
- 548 Breslow, D. K., S. Hoogendoorn, A. R. Kopp, D. W. Morgens, B. K. Vu et al., 2018 A
549 CRISPR-based screen for Hedgehog signaling provides insights into ciliary
550 function and ciliopathies. *Nat Genet.* **50**: 460-471. doi:10.1038/s41588-018-0054-
551 7
- 552 Briscoe, J., and J. Ericson J, 1999 The specification of neuronal identity by graded
553 Sonic Hedgehog signalling. *Semin Cell Dev Biol.* **10**: 353-362.
554 doi:10.1006/scdb.1999.0295
- 555 Cantagrel, V., J. L. Silhavy, S. L. Bielas, D. Swistun, S. E. Marsh et al., 2008 Mutations
556 in the cilia gene ARL13B lead to the classical form of Joubert syndrome. *Am J*
557 *Hum Genet.* **83**: 170-179. doi:10.1016/j.ajhg.2008.06.023
- 558 Casoni, F., L. Croci, F. Vincenti, P. Podini, M. Riba et al., 2020 ZFP423 regulates early
559 patterning and multiciliogenesis in the hindbrain choroid plexus. *Development.*
560 **147**: dev190173. doi:10.1242/dev.190173
- 561 Caspary, T., M. J. Garcia-Garcia, D. Huangfu, J. T. Eggenschwiler, M. R. Wyler et al.,
562 2002 Mouse Dispatched homolog1 is required for long-range, but not juxtacrine,
563 Hh signaling. *Curr Biol.* **12**: 1628-1632. doi:10.1016/s960-9822(02)01147-8
- 564 Caspary, T., C. E. Larkins, and K. V. Anderson, 2007 The graded response to Sonic
565 Hedgehog depends on cilia architecture. *Dev Cell.* **12**: 767-778.
566 doi:10.1016/j.devcel.2007.03.004
- 567 Charron, F., E. Stein, J. Jeong, A. P. McMahon, and M. Tessier-Lavigne, 2003 The
568 morphogen sonic hedgehog is an axonal chemoattractant that collaborates with

- 569 netrin-1 in midline axon guidance. *Cell*. **113**: 11-23. doi:10.1016/s0092-
570 8674(03)00199-5
- 571 Chavez, M., S. Ena, J. Van Sande, A. de Kerchove d'Exaerde, S. Schurmans et al.,
572 2015 Modulation of ciliary phosphoinositide content regulates trafficking and
573 Sonic hedgehog signaling output. *Dev Cell*. **34**: 338-350.
574 doi:10.1016/j.devcel.2015.06.016
- 575 Chiang, C., Y. Litingtung, E. Lee, K. E. Young, J. L. Corden et al., 1996 Cyclopia and
576 defective axial patterning in mice lacking Ssonic hedgehog gene function.
577 *Nature*. **383**: 407-413. Doi:10.1038/383407a0
- 578 Chih, B., P. Liu, Y. Chinn, C. Chalouni, L. G. Komuves et al., 2011 A ciliopathy complex
579 at the transition zone protects the cilia as a privileged membrane domain. *Nat*
580 *Cell Biol*. **14**: 61-72. doi:10.1038/ncb2410
- 581 Chizhikov, V. V., J. Davenport, Q. Zhang, E. K. Shih, O. A. Cabello et al., 2007 Cilia
582 proteins control cerebellar morphogenesis by promoting expansion of the granule
583 progenitor pool. *J Neurosci*. **27**: 9780-9789. doi:10.1523/JNEUROSCI.5586-
584 06.2007
- 585 Christopher, K. J., B. Wang, Y. Kong, and S. D. Weatherbee, 2012 Forward genetics
586 uncovers Transmembrane protein 107 as a novel factor required for ciliogenesis
587 and Sonic hedgehog signaling. *Dev Biol*. **368**: 382-392.
588 doi:10.1016/j.ydbio.2012.06.008
- 589 Constable, S., A. B. Long, K. A. Floyd, S. Schurmans, and T. Caspary, 2020 The ciliary
590 phosphatidylinositol phosphatase Inpp5e plays positive and negative regulatory
591 roles in Shh signaling. *Development*. **147**: dev183301. doi:10.1242/dev.183301

- 592 Consugar, M. B., V. J. Kubly, D. J. Lager, C. J. Hommerding, W. C. Wong et al., 2007
593 Molecular diagnostics of Meckel–Gruber syndrome highlights phenotypic
594 differences between MKS1 and MKS3. *Hum Genet.* **121**: 591-599.
595 doi:10.1007/s00439-007-0341-3
- 596 Dahmane, N., and A. Ruiz i Altaba, 1999 Sonic hedgehog regulates the growth and
597 patterning of the cerebellum. *Development.* **126**: 3089-3100.
- 598 Davey, M. G., I. R. Paton, Y. Yin, M. Schmidt, F. K. Bangs et al., 2006 The chicken
599 talpid3 gene encodes a novel protein essential for Hedgehog signaling. *Genes*
600 *Dev.* **20**: 1365-1377. doi:10.1101/gad.369106
- 601 Delous, M., L. Baala, R. Salomon, C. Laclef, J. Vierkotten et al., 2007 The ciliary gene
602 RPGRIP1L is mutated in cerebello-oculo-renal syndrome (Joubert syndrome type
603 B) and Meckel syndrome. *Nat Genet.* **39**: 875-881. doi:10.1038/ng2039
- 604 Deshpande, O., R. Z. Lara, O. R. Zhang, D. Concepcion, and B. A. Hamilton, 2020
605 ZNF423 patient variants, truncations, and in-frame deletions in mice define an
606 allele-dependent range of midline brain abnormalities. *PLoS Genet.* **16**:
607 e1009017. doi:10.1371/journal.pgen.1009017
- 608 Doherty, D., 2009 Joubert syndrome: Insights into brain development, cilium biology,
609 and complex disease. *Semin Pediatr Neurol.* **16**: 143-154.
610 doi:10.1016/j.spen.2009.06.002
- 611 Dowdle, W. E., J. F. Robinson, A. Kneist, M. S. Sirerol-Piquer, S. G. M. Frints et al.,
612 2011 Disruption of a ciliary B9 protein complex causes Meckel syndrome. *Am J*
613 *Hum Genet.* **89**: 94-110. doi:10.1016/j.ajhg.2011.06.003

- 614 Fabre, P. J., T. Shimogori, and F. Charron, 2010 Segregation of ipsilateral retinal
615 ganglion cell axons at the optic chiasm requires the Shh receptor Boc. *J*
616 *Neurosci.* **30**: 266-275. doi:10.1523/JNEUROSCI.2778-09.2010
- 617 Ferent, J., S. Constable, E. D. Gigante, P. T. Yam, L. E. Mariani et al., 2019 The ciliary
618 protein Arl13b functions outside of the primary cilium in Shh-mediated axon
619 guidance. *Cell Rep.* **29**: 3356-3366.e3353. doi:10.1016/j.celrep.2019.11.015
- 620 Fink, A. J., C. Englund, R. A. M. Daza, D. Pham, C. Lau et al., 2006 Development of
621 the deep cerebellar nuclei: Transcription factors and cell migration from the
622 rhombic lip. *J Neurosci.* **26**: 3066-3076. doi:10.1523/JNEUROSCI.5203-05.2006
- 623 Frikstad, K-A. M., E. Molinari, M. Thoresen, S. A. Ramsbottom, F. Hughes et al., 2019
624 A CEP104-CSPP1 complex is required for formation of primary cilia competent in
625 Hedgehog signaling. *Cell Rep.* **28**: 1907-1922.e6
626 doi:10.1016/j.celrep.2019.07.025
- 627 Garcia-Gonzalo, F. R., K. C. Corbit, M. S. Sirerol-Piquer, G. Ramaswami, E. A. Otto et
628 al., 2011 A transition zone complex regulates mammalian ciliogenesis and ciliary
629 membrane composition. *Nat Genet.* **43**: 776-784. doi:10.1038/ng.891
- 630 Garcia-Gonzalo, F. R., S. C. Phua, E. C. Roberson, G. Garcia 3rd, M. Abedin et al.,
631 2015 Phosphoinositides regulate ciliary protein trafficking to modulate Hedgehog
632 signaling. *Dev Cell.* **34**: 400-409. doi:10.1016/j.devcel.2015.08.001
- 633 Gaudet, M., A-G. Fara, I. Beritognolo, and M. Sabatti, 2009 Allele-specific PCR in SNP
634 genotyping. *Methods Mol Biol.* **578**: 415-424. doi:10.1007/978-1-60327-411-1_26

- 635 Gigante, E. D., M. R. Taylor, A. A. Ivanova, R. A. Kahn, and T. Caspary, 2020. ARL13B
636 regulates Sonic hedgehog signaling from outside primary cilia. *eLife*. **9**: e50434.
637 doi:10.7554/eLife.50434
- 638 Goebbels, S., I. Bormuth, U. Bode, O. Hermanson, M. H. Schwab et al., 2006 Genetic
639 targeting of principal neurons in neocortex and hippocampus of NEX-Cre mice.
640 *Genesis*. **44**: 611-621. doi:10.1002/dvg.20256
- 641 Gotthardt, K., M. Lokaj, C. Koerner, N. Falk, A. Giessl et al., 2015 A G-protein
642 activation cascade from Arl13b to Arl3 and implications for ciliary targeting of
643 lipidated proteins. *eLife*. **4**: e11859. doi:10.7554/eLife.11859
- 644 Guo, J., J. M. Otis, S. K. Suci, C. Catalano, L. Xing et al., 2019 Primary cilia signaling
645 promotes axonal tract development and is disrupted in Joubert syndrome-related
646 disorders models. *Dev Cell*. **51**: 759-774 e755. doi:10.1016/j.devcel.2019.11.005
- 647 Hagemann, A. I. H., and S. Scholpp, 2012 The tale of the three brothers – Shh, Wnt,
648 and Fgf during development of the thalamus. *Front Neurosci*. **6**: 76.
649 doi:10.3389/fnins.2012.00076
- 650 Haldipur, P., K. A. Aldinger, S. Bernardo, M. Deng, A. E. Timms et al., 2019
651 Spatiotemporal expansion of primary progenitor zones in the developing human
652 cerebellum. *Science*. **366**: 454-460. Doi: 10.1126/science.aax7526
- 653 Hata, A., J. Seoane, G. Lagna, E. Montalvo, A. Hemmati-Brivanlou et al., 2000 OAZ
654 uses distinct DNA- and protein-binding zinc fingers in separate BMP-Smad and
655 Olf signaling pathways. *Cell*. **100**: 229-240. doi:10.1016/s0092-8674(00)81561-5
- 656 Hazen, V. M. , M. G. Andrews, L. Umans, E. B. Crenshaw 3rd, A. Zwijsen et al., 2012
657 BMP receptor-activated Smads confer diverse functions during the development

- 658 of the dorsal spinal cord. *Dev Biol.* **367**: 216-227.
- 659 doi:10.1016/j.ydbio.2012.05.014
- 660 Heydemann, A., L. C. Nguyen, and E. B. Crenshaw 3rd, 2001 Regulatory regions from
661 the Brn4 promoter direct LACZ expression to the developing forebrain and neural
662 tube. *Brain Res Dev Brain Res.* **128**: 83-90. doi:10.1016/s0165-3806(01)00137-7
- 663 Hopp, K., C. M. Heyer, C. J. Hommerding, S. A. Henke, J. L. Sundsbak et al., 2011
664 B9D1 is revealed as a novel Meckel syndrome (MKS) gene by targeted exon-
665 enriched next-generation sequencing and deletion analysis. *Hum Mol Genet.* **20**:
666 2524-2534. doi:10.1093/hmg/ddr151
- 667 Horner, V. L., and T. Caspary, 2011 Disrupted dorsal neural tube BMP signaling in the
668 cilia mutant Arl13b hnn stems from abnormal Shh signaling. *Dev Biol.* **355**: 43-
669 54. doi:10.1016/j.ydbio.2011.04.019
- 670 Huang, S., J. Laoukili, M. T. Epping, J. Koster, M. Hölzel et al., 2009 ZNF423 is
671 critically required for retinoic acid-induced differentiation and is a marker of
672 neuroblastoma outcome. *Cancer Cell.* **15**: 328-340.
673 doi:10.1016/j.ccr.2009.02.023
- 674 Huangfu, D., A. Liu, A. S. Rakeman, N. S. Murcia, L. Niswander et al., 2003 Hedgehog
675 signalling in the mouse requires intraflagellar transport proteins. *Nature.* **426**: 83-
676 87. doi:10.1038/nature02061
- 677 Humbert, M. C., K. Weihbrecht, C. C. Searby, Y. Li, R. M. Pope et al., 2012 ARL13B,
678 PDE6D, and CEP164 form a functional network for INPP5E ciliary targeting. *Proc*
679 *Natl Acad Sci U S A.* **109**: 19691-19696. doi:10.1073/pnas.1210916109

- 680 Hynes, A. M., R. H. Giles, S. Srivastava, L. Eley, J. Whitehead et al., 2014 Murine
681 Joubert syndrome reveals Hedgehog signaling defects as a potential therapeutic
682 target for nephronophthisis. *Proc Natl Acad Sci U S A.* **111**: 9893-9898.
683 doi:10.1073/pnas.1322373111
- 684 Ivanova, A. A., T. Caspary, N. T. Seyfried, D. M. Duong, A. B. West et al., 2017
685 Biochemical characterization of purified mammalian ARL13B protein indicates
686 that it is an atypical GTPase and ARL3 guanine nucleotide exchange factor
687 (GEF). *J Biol Chem.* **292**: 11091-11108. doi:10.1074/jbc.M117.784025
- 688 Kenney, A. M., and D. H. Rowitch, 2000 Sonic hedgehog promotes G(1) cyclin
689 expression and sustained cell cycle progression in mammalian neuronal
690 precursors. *Mol Cell Biol.* **20**: 9055-9067. doi:10.1128/mcb.20.23.9055-
691 9067.2000
- 692 Lan, Y., and R. Jiang, 2009 Sonic hedgehog signaling regulates reciprocal epithelial-
693 mesenchymal interactions controlling palatal outgrowth. *Development.* **136**:
694 1387-1396. doi:10.1242/dev.028167
- 695 Lancaster, M. A., D. J. Gopal, J. Kim, S. N. Saleem, J. L. Silhavy et al., 2011 Defective
696 Wnt-dependent cerebellar midline fusion in a mouse model of Joubert syndrome.
697 *Nat Med.* **17**: 726-731. doi:10.1038/nm.2380
- 698 Lipinski, R. J., C. Song, K. K. Sulik, J. L. Everson, J. J. Gipp et al., 2010 Cleft lip and
699 palate results from Hedgehog signaling antagonism in the mouse: Phenotypic
700 characterization and clinical implications. *Birth Defects Res A Clin Mol Teratol.*
701 **88**: 232-240. doi:10.1002/bdra.20656

- 702 Mariani, L. E., M. F. Bijlsma, A. A. Ivanova, S. K. Suciu, R. A. Kahn et al., 2016 Arl13b
703 regulates Shh signaling from both inside and outside the cilium. *Mol Biol Cell*. **27**:
704 3780-3790. doi:10.1091/mbc.E16-03-0189
- 705 Miertzschke, M., C. Koerner, M. Spoerner, and A. Wittinghofer, 2014 Structural insights
706 into the small G-protein Arl13b and implications for Joubert syndrome. *Biochem*
707 *J*. **457**: 301-311. doi:10.1042/BJ20131097
- 708 Munoz-Estrada, J., and R. J. Ferland, 2019 Ahi1 promotes Arl13b ciliary recruitment,
709 regulates Arl13b stability and is required for normal cell migration. *J Cell Sci*.
710 **132**: jcs230680. doi:10.1242/jcs.230680
- 711 Nolan-Stevaux, O., J. Lau, M. L. Truitt, G. C. Chu, M. Hebrok et al., 2009 Gli1 is
712 regulated through Smoothed-independent mechanisms in neoplastic
713 pancreatic ducts and mediates PDAC cell survival and transformation. *Genes*
714 *Dev*. **23**: 24-36. doi:10.1101/gad.1753809
- 715 Onimaru, H., Y. Kumagawa, and I. Homma, 2006 Respiration-related rhythmic activity
716 in the rostral medulla of newborn rats. *J Neurophysiol*. **96**: 55-61.
717 doi:10.1152/jn.01175.2005
- 718 Otto, E. A., K. Tory, M. Attanasio, W. Zhou, M. Chaki et al, 2009 Hypomorphic
719 mutations in meckelin (MKS3/TMEM67) cause nephronophthisis with liver
720 fibrosis (NPHP11). *J Med Genet*. **46**: 663-670. doi:10.1136/jmg.2009.066613
- 721 Parisi, M. A, 2019 The molecular genetics of Joubert syndrome and related ciliopathies:
722 The challenges of genetic and phenotypic heterogeneity. *Transl Sci Rare Dis*. **4**:
723 25-49. doi:10.3233/TRD-190041

- 724 Parisi, M. A., D. Doherty, P. F. Chance, and I. A. Glass, 2007 Joubert syndrome (and
725 related disorders) (OMIM 213300). *Eur J Hum Genet.* **15**: 511-521.
726 doi:10.1038/sj.ejhg.5201648
- 727 Pasqualato, S., L. Renault, and J. Cherfils, 2002. Arf, Arl, Arp and Sar proteins: A family
728 of GTP-binding proteins with a structural device for 'front-back' communication.
729 *EMBO Rep.* **3**: 1035-1041. doi:10.1093/embo-reports/kvf221
- 730 Poretti, A., E. Boltshauser, T. Loenneker, E. M. Valente, F. Brancati et al., 2007
731 Diffusion tensor imaging in Joubert syndrome. *AJNR Am J Neuroradiol.* **28**:
732 1929-1933. doi:10.3174/ajnr.A0703
- 733 Quisling, R. G., A. J. Barkovich, and B. L. Maria, 1999 Magnetic resonance imaging
734 features and classification of central nervous system malformations in Joubert
735 syndrome. *J Child Neurol.* **14**: 628-635. doi:10.1177/088307389901401002
- 736 Rafiullah, R., A. B. Long, A. A. Ivanova, H. Ali, S. Berkel et al., 2017 A novel
737 homozygous ARL13B variant in patients with Joubert syndrome impairs its
738 guanine nucleotide-exchange factor activity. *Eur J Hum Genet.* **25**: 1324-1334.
739 doi:10.1038/s41431-017-0031-0
- 740 Ramsbottom, S. A., P. E. Thelwall, K. M. Wood, G. J. Clowry, L. A. Devlin et al., 2020
741 Mouse genetics reveals Barttin as a genetic modifier of Joubert syndrome. *Proc*
742 *Natl Acad Sci U S A.* **117**: 1113-1118. doi:10.1073/pnas.1912602117
- 743 Reiter, J. F., and W. C. Skarnes, 2006 Tectonic, a novel regulator of the Hedgehog
744 pathway required for both activation and inhibition. *Genes Dev.* **20**: 22-27.
745 doi:10.1101/gad.1363606

- 746 Roberson, E. C., W. E. Dowdle, A. Ozanturk, F. R. Garcia-Gonzalo, C. Li et al., 2015
747 TMEM231, mutated in orofacioidigital and Meckel syndromes, organizes the
748 ciliary transition zone. *J Cell Biol.* **209**: 129-142. doi:10.1083/jcb.201411087
- 749 Sanchez-Arrones, L., F. Nieto-Lopez, C. Sanchez-Camacho, M. I. Carreres, E. Herrera
750 et al., 2013 Shh/Boc signaling is required for sustained generation of ipsilateral
751 projecting ganglion cells in the mouse retina. *J Neurosci.* **33**: 8596-8607.
752 doi:10.1523/JNEUROSCI.2083-12.2013
- 753 Sang, L., J. J. Miller, K. C. Corbit, R. H. Giles, M. J. Brauer et al., 2011 Mapping the
754 NPHP-JBTS-MKS protein network reveals ciliopathy disease genes and
755 pathways. *Cell.* **145**: 513-528. doi:10.1016/j.cell.2011.04.019
- 756 Schindelin, J., I. Arganda-Carreras, E. Frise, V. Kaynig, M. Longair et al., 2012 Fiji: an
757 open-source platform for biological-image analysis. *Nat Methods.* **9**: 676-682.
758 doi:10.1038/nmeth.2019
- 759 Schrick, J. J., P. Vogel, A. Abuin, B. Hampton, and D. S. Rice, 2006 ADP-ribosylation
760 factor-like 3 is involved in kidney and photoreceptor development. *Am J Pathol.*
761 **168**: 1288-1298. doi:10.2353/ajpath.2006.050941
- 762 Shaheen, R., K. Szymanska, B. Basu, N. Patel, N. Ewida et al., 2016 Characterizing
763 the morbid genome of ciliopathies. *Genome Biol.* **17**: 242. doi:10.1186/s13059-
764 016-1099-5
- 765 Srour, M., F. F. Hamdan, J. A. Schwartzenuber, L. Patry, L. H. Ospina et al., 2012
766 Mutations in TMEM231 cause Joubert syndrome in French Canadians. *J Med*
767 *Genet.* **49**: 636-641. doi:10.1136/jmedgenet-2012-101132

- 768 Su, C-Y., S. N. Bay, L. E. Mariani, M. J. Hillman, and T. Caspary, 2012 Temporal
769 deletion of *Arl13b* reveals that a mispatterned neural tube corrects cell fate over
770 time. *Development*. **139**: 4062-4071. doi:10.1242/dev.082321
- 771 Thomas, S., V. Cantagrel, L. Mariani, V. Serre, J-E. Lee et al., 2015 Identification of a
772 novel *ARL13B* variant in a Joubert syndrome-affected patient with retinal
773 impairment and obesity. *Eur J Hum Genet*. **23**: 621-627.
774 doi:10.1038/ejhg.2014.156
- 775 Thomas, S., M. Legendre, S. Saunier, B. Bessières, C. Alby et al., 2012 *TCTN3*
776 mutations cause Mohr-Majewski syndrome. *Am J Hum Genet*. **91**: 372-378.
777 doi:10.1016/j.ajhg.2012.06.017
- 778 Tran, P. V., C. J. Haycraft, T. Y Besschetnova, A. Turbe-Doan, R. W. Stottmann et al.,
779 2008 *THM1* negatively modulates mouse sonic hedgehog signal transduction
780 and affects retrograde intraflagellar transport in cilia. *Nat Genet*. **40**: 403-410.
781 doi:10.1038/ng.105
- 782 Valente, E. M., F. Brancati, and B. Dallapiccola, 2008 Genotypes and phenotypes of
783 Joubert syndrome and related disorders. *Eur J Med Genet*. **51**: 1-23.
784 doi:10.1016/j.ejmg.2007.11.003
- 785 Valente, E. M., C. V. Logan, S. Mougou-Zerelli, J. H. Lee, J. L. Silhavy et al., 2010
786 Mutations in *TMEM216* perturb ciliogenesis and cause Joubert, Meckel and
787 related syndromes. *Nat Genet*. **42**: 619-625. doi:10.1038/ng.594
- 788 Vierkotten, J., R. Dildrop, T. Peters, B. Wang, and U. Rütther, 2007 *Ftm* is a novel basal
789 body protein of cilia involved in *Shh* signaling. *Development*. **134**: 2569-2577.
790 doi:10.1242/dev.003715

- 791 Weatherbee, S. D., L. A. Niswander, and K. V. Anderson, 2009 A mouse model for
792 Meckel syndrome reveals Mks1 is required for ciliogenesis and Hedgehog
793 signaling. *Hum Mol Genet.* **18**: 4565-4575. doi:10.1093/hmg/ddp422
- 794 Wechsler-Reya, R. J., and M. P. Scott, 1999 Control of neuronal precursor proliferation
795 in the cerebellum by Sonic Hedgehog. *Neuron.* **22**: 103-114. doi:10.1016/s0896-
796 6273(00)80682-0
- 797 Wu, C., M. Yang, J. Li, C. Wang, T. Cao et al., 2014 Talpid3-binding centrosomal
798 protein Cep120 is required for centriole duplication and proliferation of cerebellar
799 granule neuron progenitors. *PLoS One.* **9**: e107943.
800 doi:10.1371/journal.pone.0107943
- 801 Yachnis, A. T., and L. B. Rorke, 1999 Neuropathology of Joubert syndrome. *J Child*
802 *Neurol.* **14**: 655-659. doi:10.1177/088307389901401006
- 803 Zhang, X. M., M. Ramalho-Santos, and A. P. McMahon, 2001 Smoothed mutants
804 reveal redundant roles for Shh and Ihh signaling including regulation of L/R
805 symmetry by the mouse node. *Cell.* **106**: 781-792.

806

807 **Figure legends**

808 **Figure 1: SCPs lacking *Arl13b* or *Smo* fail to project to the dorsal thalamus.** (A-C)
809 Schematics of injections and fluorescent tracer diffusion shown horizontally (A) or
810 sagittally (B-C). (A) Red dashed arrow depicts dye path in a successful injection from
811 injection site (red X) caudal through the brain and across the midline and into the
812 contralateral cerebellar DCN (red arrowhead). Grey background boxes indicate area of
813 subsequent images: the injection site (INJ) and cerebellum (DCN). (D-I) Representative
814 images of dorsal (D, F, H) or ventral (E, G, I) thalamus injection site (top panel) and

815 cerebellum (middle panel) with the DCN in hatched white circle and magnified (bottom
816 panel) with recoloring to black and white to aid visualization. The retrograde fluorescent
817 tracer is pink-red and sections are stained with DAPI (blue). Numbers indicate the
818 number of positively stained DCN clusters (DCN traced) out of the total number of
819 injected animals. Note that no tracing was observed on ipsilateral side to injection. (D,
820 E) Fluorescent tracer injection in *Smo^{fl/+}; Arl13b^{fl/+}; Nex-Cre* control animals resulted in
821 contralateral DCN staining in (D) 6/8 dorsal thalamus injections and (E) 8/11 ventral
822 thalamus injections. (F, G) Fluorescent tracer injection in *Smo^{Nex-Cre}* animals resulted in
823 contralateral DCN staining in (F) 0/6 dorsal thalamus injections (Fisher's exact test, two-
824 tailed, significant difference, $P=0.0097$) and (G) 4/4 ventral thalamus injections (not
825 significant (ns), $P=0.5165$). (H, I) Fluorescent tracer injection in *Arl13b^{Nex-Cre}* animals
826 resulted in contralateral DCN staining in (H) 1/7 dorsal thalamus injections (significant
827 difference, $P=0.0406$) and (I) 4/4 ventral thalamus injections (ns, $P=0.5165$).

828

829 **Figure 2: SCPs expressing cilia-excluded ARL13B^{V358A} project normally to both**
830 **the dorsal and ventral thalamus.** (A-D) Representative images of dorsal (A, C) or
831 ventral (B, D) thalamus injection site (top panel) and cerebellum (middle panel) with the
832 DCN in hatched white circle and magnified (bottom panel) with recoloring to black and
833 white to aid visualization. Numbers indicate the number of positively stained DCN
834 clusters out of the total number of injected animals. Note that no tracing was observed
835 on the injection's ipsilateral side. (A, B) Fluorescent tracer injection in *Arl13b^{V358A/+}*
836 control animals resulted in contralateral DCN staining in (A) 3/3 dorsal thalamus
837 injections and (B) 5/5 ventral thalamus injections. (C-D) Fluorescent tracer injection in

838 *Arl13b*^{V358A/V358A} animals resulted in contralateral DCN staining in (C) 3/3 dorsal
839 thalamus injections (Fisher's exact test, two-tailed, ns, P>0.9999) and (D) 5/5 ventral
840 thalamus injections (ns, P>0.9999).

841

842 **Figure 3: SCPs expressing JS allele *Arl13b*^{R79Q} project normally to both the dorsal**
843 **and ventral thalamus** (A-D) Representative images of dorsal (A, C) or ventral (B, D)
844 thalamus injection site (top panel) and cerebellum (middle panel) with the DCN in
845 hatched white circle and magnified (bottom panel) with recoloring to black and white to
846 aid visualization. Numbers indicate the number of positively stained DCN clusters out of
847 the total number of injected animals. Note that no tracing was observed on the
848 injection's ipsilateral side. (A, B) Fluorescent tracer injection in *Arl13b*^{R79Q/+} control
849 animals resulted in contralateral DCN staining in (A) 4/4 dorsal thalamus injections and
850 (B) 3/3 ventral thalamus injections. (C-D) Fluorescent tracer injection in *Arl13b*^{R79Q/R79Q}
851 animals resulted in contralateral DCN staining in (C) 3/3 dorsal thalamus injections
852 (Fisher's exact test, two-tailed, ns, P>0.9999) and (D) 3/4 ventral thalamus injections
853 (ns, P>0.9999).

854

855 **Figure 4: Mouse embryos expressing JS allele *Arl13b*^{R79Q} display normal cell**
856 **patterning in the neural tube.** Shh, Olig2 and Pax6 staining of E10.5 *Arl13b*^{+/+} (n=3),
857 *Arl13b*^{R79Q/R79Q} (n=3), *Arl13b*^{R79Q/Δ} (n=3), and *Arl13b*^{Δ/Δ} (n=3) mouse neural tubes. Scale
858 bar = 100 micrometers. (A-D) Shh is visible in the notochord and floorplate of (A)
859 *Arl13b*^{+/+}, (B) *Arl13b*^{R79Q/R79Q} and (C) *Arl13b*^{R79Q/Δ} neural tubes but absent from the
860 floorplate of (D) *Arl13b*^{Δ/Δ} embryos. (E-H) Olig2 stains the pMN domain in (E) *Arl13b*^{+/+},

861 (F) *Arl13b*^{R79Q/R79Q} and (G) *Arl13b*^{R79Q/Δ} embryos and stains an expanded domain in (H)
862 *Arl13b*^{ΔΔ} embryos. (I-L) Pax6 expression is visible in the dorsal neural tube in (I)
863 *Arl13b*^{+/+}, (J) *Arl13b*^{R79Q/R79Q} and (K) *Arl13b*^{R79Q/Δ} neural tubes but shifted dorsally in (L)
864 *Arl13b*^{ΔΔ} neural tubes.

865

866 **Figure 5: *Arl13b*^{R79Q} mutation does not affect cerebellar size.** (A) Representative
867 surface-facing images of cerebella from control and *Arl13b*^{R79Q/R79Q} mutant mice.
868 Scalebar = 1mm. (B) Ratio of *Arl13b*^{R79Q/R79Q} mutant to control cerebellar width
869 measured from surface views of sex- and age-matched pairs showed no significant
870 difference from the hypothetical ratio of 1 (one-sample t-test: female p=0.9524, male
871 p=0.5244). (C) Ratio of *Arl13b*^{R79Q/R79Q} mutant to control vermis width measured at
872 lobule VII showed no significant difference from hypothetical ratio of 1 (one-sample t-
873 test: female p=0.4895, male p=0.9376). Each dot represents a pair of sex- and age-
874 matched animals.

875

876 **Figure 6: Pan-neuronal deletion of *Arl13b* results in a small cerebellum.** (A)
877 Representative images of cerebella from control and *Arl13b*^{Bm4-Cre} mutant mice.
878 Scalebar = 1mm. (B) The ratio of *Arl13b*^{Bm4-Cre} mutant to control cerebellar width was
879 reduced 6% in both female and males compared to a hypothetical ratio of 1 (one-
880 sample t-test: female p=0.0111, male p=0.0144). (C) The ratio of *Arl13b*^{Bm4-Cre} mutant to
881 control cerebellar vermis width was reduced 27% in female and 33% in male age
882 matched pairs (one-sample t-test: female p<0.0001, male p<0.0001). Each dot
883 represents a pair of sex- and age-matched animals.

884

885 **Figure 7: Mice expressing cilia-excluded *Arl13b*^{V358A} have cerebella of normal**

886 **size.** (A) Representative images of cerebella from control and *Arl13b*^{V358A/V358A} mutant

887 mice. Scalebar = 1mm. (B) Ratio of *Arl13b*^{V358A/V358A} mutant to control cerebellar width

888 measured in same-sex age-matched pairs of mice showed no significant difference from

889 the hypothetical ratio of 1 (one-sample t-test: female p=0.6885, male p=0.2704). (C)

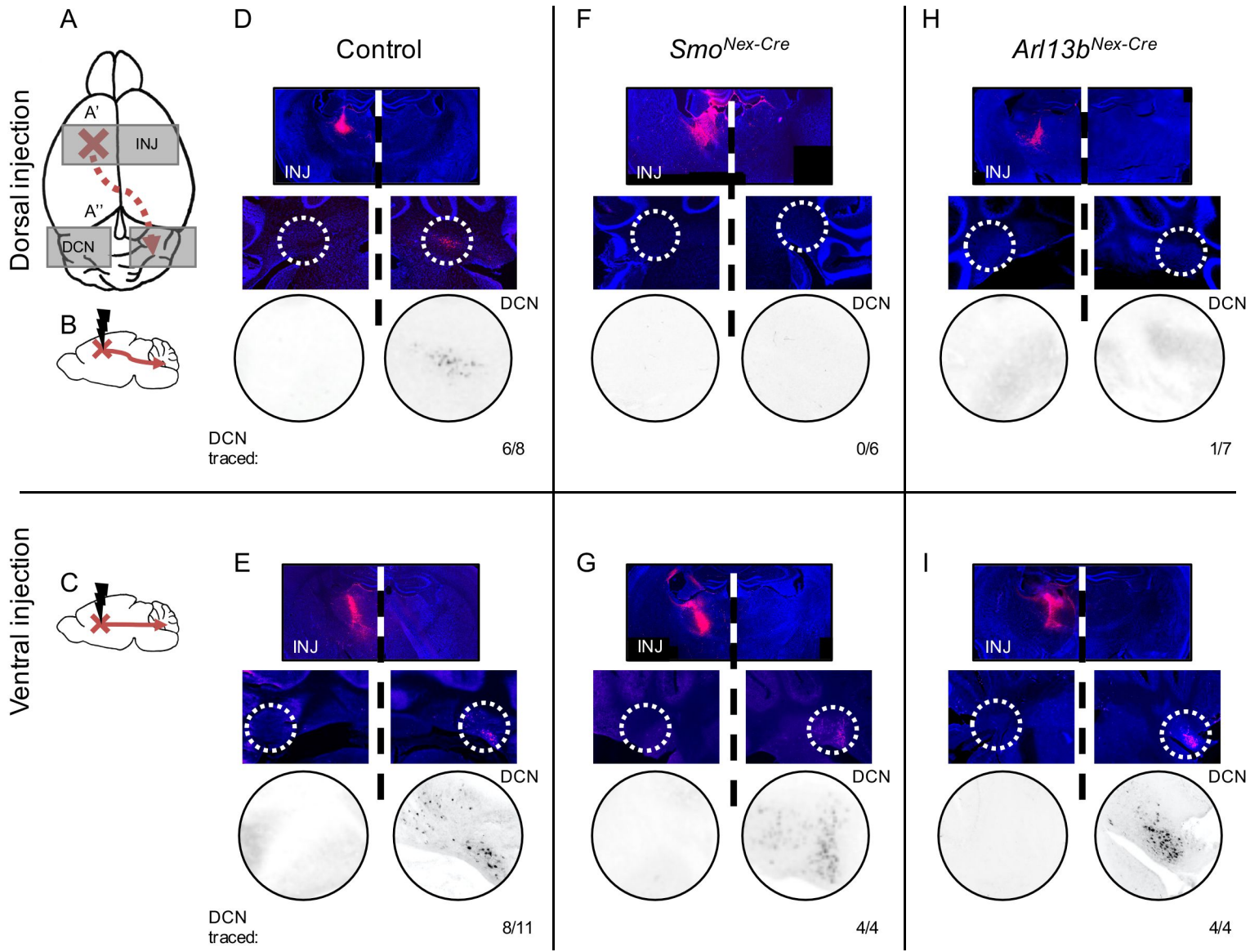
890 Ratio of *Arl13b*^{V358A/V358A} mutant to control vermis width measured at lobule VII showed

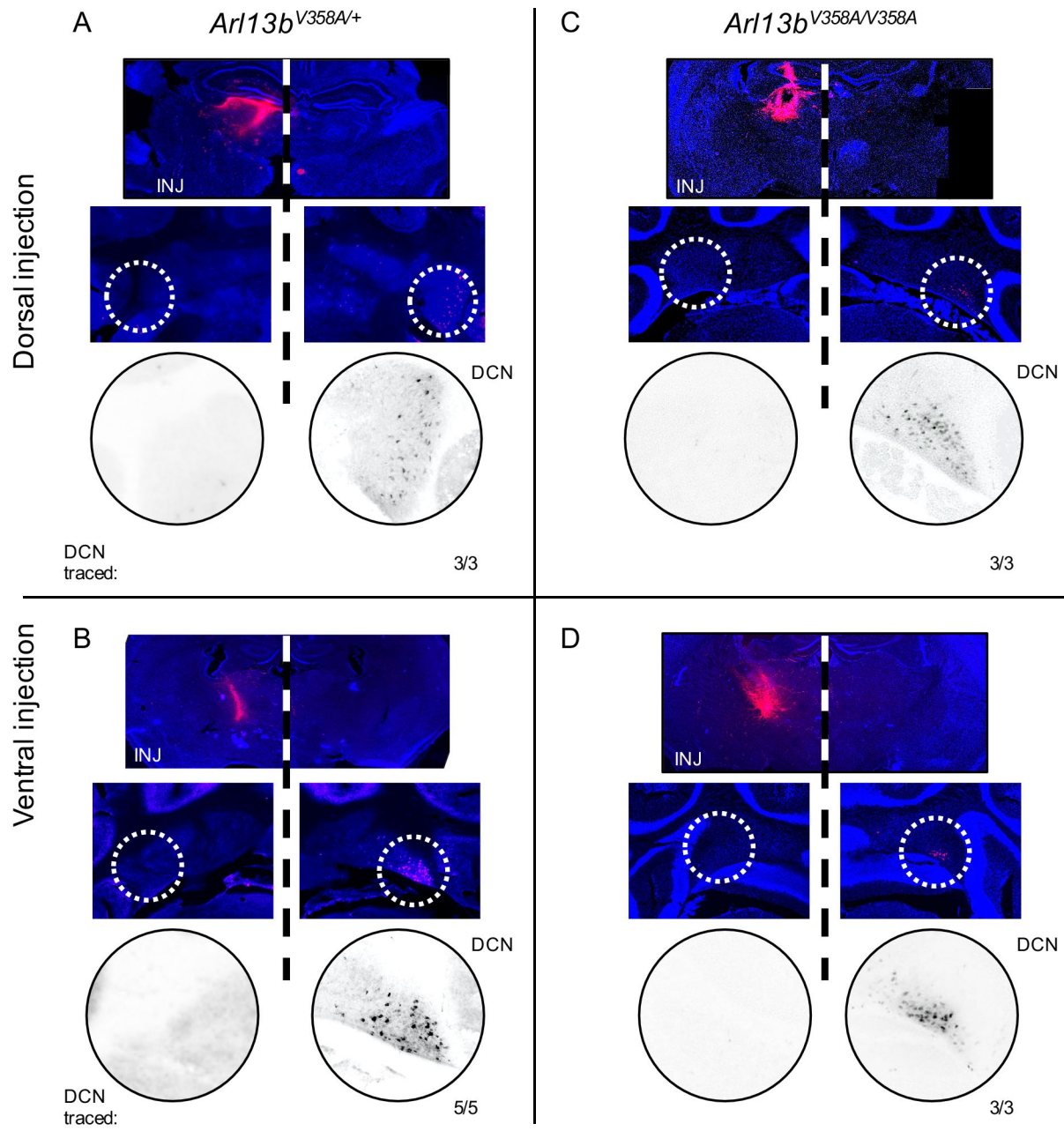
891 no significant difference from hypothetical ratio of 1 (one-sample t-test: female

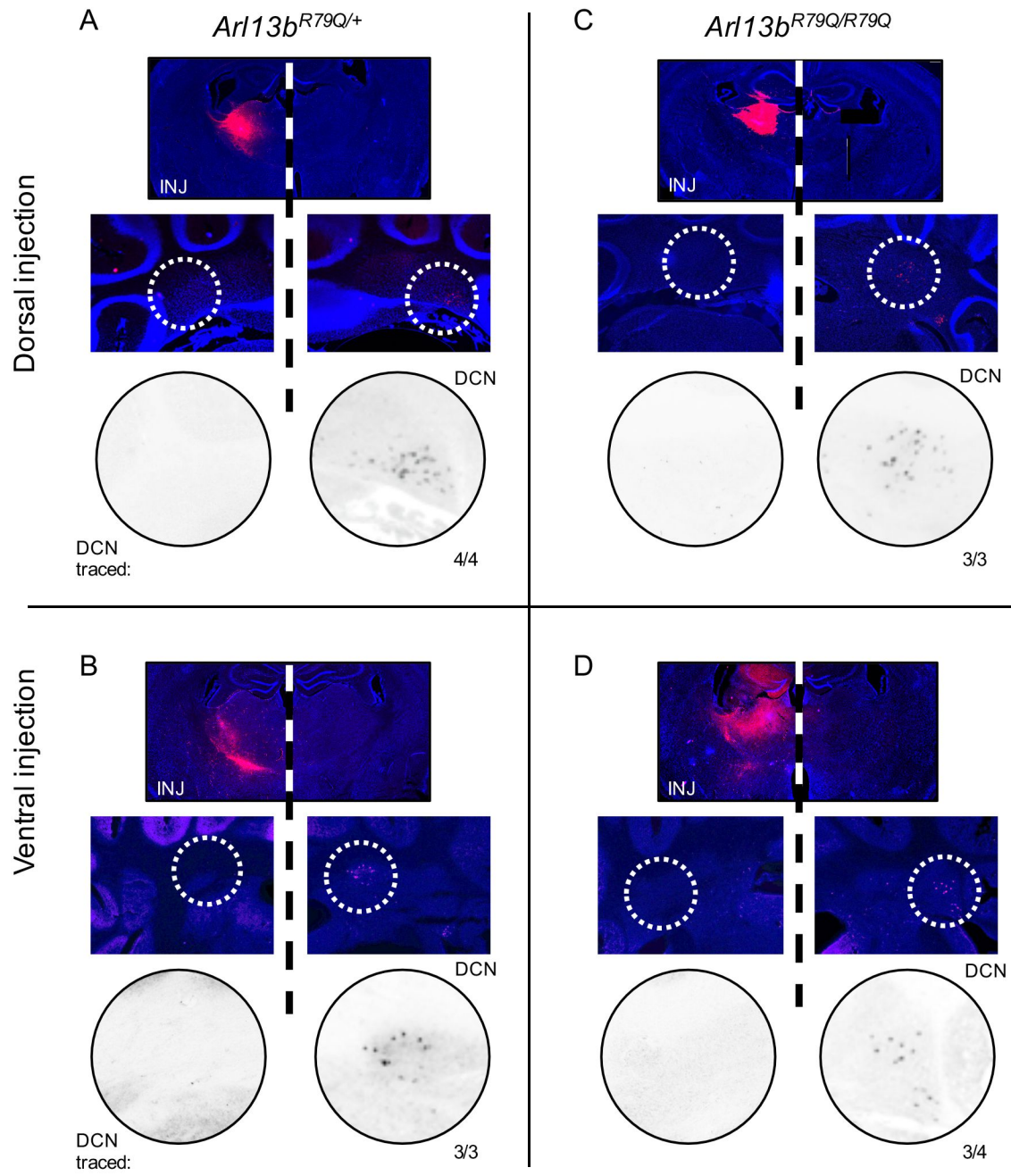
892 p=0.4246, male p=0.0519). Each dot represents a pair of sex- and age-matched

893 animals.

894







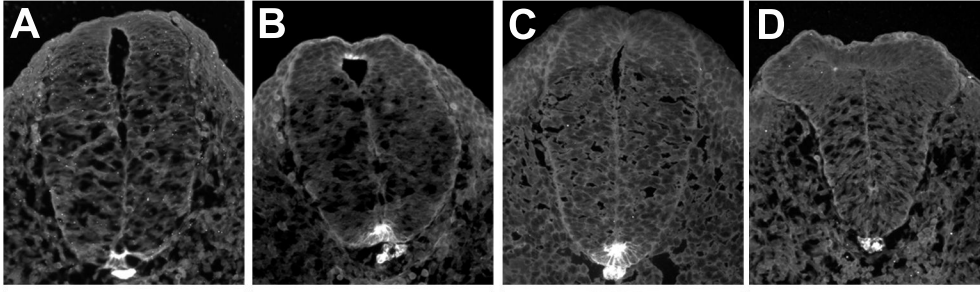
Arl13b^{+/+}

Arl13b^{R79Q/R79Q}

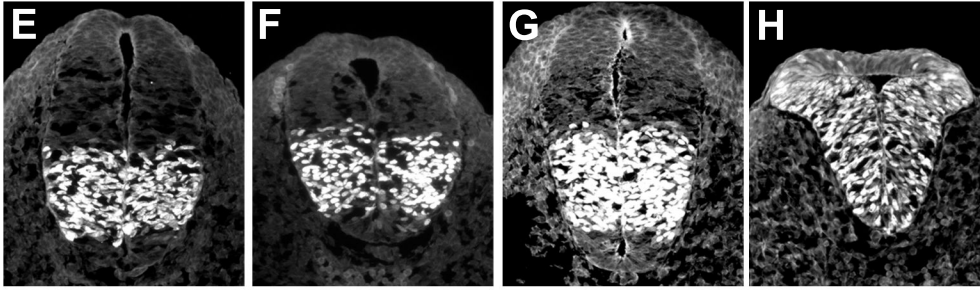
Arl13b^{R79Q/Δ}

Arl13b^{Δ/Δ}

Shh



Olig2



Pax6

